

Contents lists available at ScienceDirect

International Journal of Mechanical Sciences

journal homepage: www.elsevier.com/locate/ijmecsci



Analytical model for large deflection bending of helically stranded electrical wires



Sai Siddhartha Vemula ^{a,b}, Mingshi Ji ^b, Leon M. Headings ^{a,b}, Kushal Gargesh ^c, Soheil Soghrati ^{b,d}, Marcelo J. Dapino ^{a,b,*}

- ^a NSF IUCRC on Smart Vehicle Concepts, The Ohio State University, Columbus, OH 43210, USA
- ^b Department of Mechanical and Aerospace Engineering, The Ohio State University, Columbus, OH 43210, USA
- c Honda R&D Americas, Raymond, OH 43067, USA
- $^{
 m d}$ Department of Materials Science and Engineering, The Ohio State University, Columbus, OH 43210, USA

ARTICLE INFO

Keywords: Electrical wires Wire harness Large deflection bending Wire rope

ABSTRACT

An analytical model is presented to calculate the elasto-plastic bending response of electrical wires subjected to large deflections. Electrical wires are defined as helically wound conductors enclosed in polymer insulation. For modeling purposes, the conductor layout in a wire's cross section is estimated using a packing algorithm. Euler-Bernoulli beam theory describes the overall wire bending behavior; the conductors' stick-slip behavior is modeled based on Coulomb's friction law. In the plastic region, the conductors are modeled as laminated composite beams. A cantilever bending setup is used to characterize the force displacement response of wires with different diameters, number of conductors, beam lengths, and conductor cross sections. The model parameters are calibrated to ensure that the force-displacement calculations are within the 95% confidence interval of the test data.

1. Introduction

Automobiles have multiple electronic, electrical, and electromechanical systems connected by a network of wire harnesses. Issues related to wire harnesses are a root cause of a significant number of customer reported problems [1]. Additionally, increasing vehicle electrification due to technological advances has increased the complexity of wire harnesses [2]. This has increased the demand for reliability of wire harnesses. Shortened development periods and reduced number of prototypes has also called for a greater efficiency in harness design. This can be achieved with digital manufacturing of wire harnesses to identify and mitigate any performance issues that may arise during and after manufacturing. However, current commercial software is intrinsically inaccurate for mechanical modeling of wire harness networks since they typically assume linear elasticity, whereas in practice, harnesses are complex multi-material structures that undergo elasto-plastic deformations. Hence, there is a need to accurately model the harness components for use in digital manufacturing applications. Digital manufacturing can also help to identify the effects of variability in harness features such as excess harness lengths or insufficient tape layers, neither of which damage the harness but can cause unwanted noise due to rattling.

A wire harness is an assembly of electrical wires, protective conduits, insulation tape, mounting clips, and electrical connectors. Electrical wires are key building blocks of wire harnesses and a starting point for addressing the complex structure of wire harnesses. A typical electrical wire is made by helically winding conductors around a core in one or multiple layers, and then encasing them in polymeric insulation (Fig. 1). Harnesses are predominantly subjected to bending loads during the assembly process [3], so this work focuses on modeling the response of wires subjected to such loads.

Costello [4] proposed a model for bending of wire ropes with single layers, which posits that the bending stiffness reaches a minimum value corresponding to the slip state. This model was generalized for wires with complex cross sections by Velinsky [5]. However, neither of these models includes the effect of interlayer friction. Lanteigne [6] formulated a general stiffness matrix for aluminum conductor steel reinforced (ACSR) cables subjected to bending, torsion, and elongation which includes only the contribution of radial force to interlayer friction. Papailiou [7] presented a model for bending of ACSR cables taking into account interlayer friction and derived a moment-curvature relationship. Hong et al. [8] have modified the model by including the change in interlayer lay angle for calculating the radial contact forces.

^{*} Corresponding author at: Department of Mechanical and Aerospace Engineering, The Ohio State University, Columbus, OH 43210, USA. *E-mail address*: dapino.1@osu.edu (M.J. Dapino).

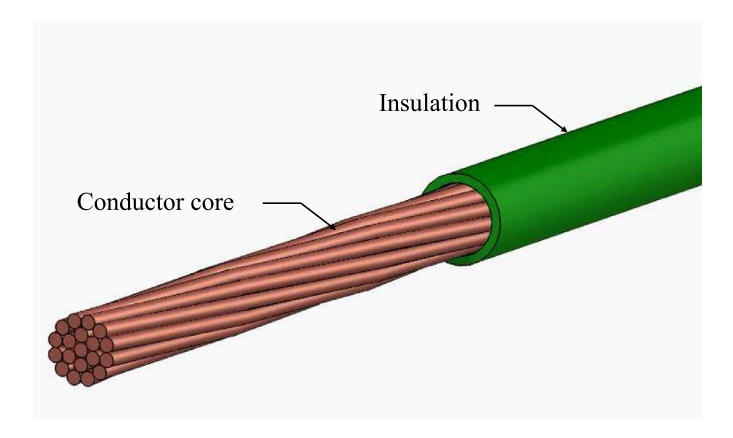


Fig. 1. Architecture of a typical helically-wound, stranded electrical wire modeled in this paper.

Inagaki et al. [9] extended Papailiou's model to second-order helical cables and modeled the effect of axial and torsional forces on the bending moment of wire conductors, incorporating a model for the contact between insulation and conductors. Foti and Martinelli [10] extended this model by including the effect of residual radial contact forces between layers and also proposing a substantially different approach to evaluate the axial force in the wires. Another extension of Papailiou's model is presented in Foti and Martinelli [11], which accounts for the coupled axial-bending behavior of wire ropes. Jiang [12] presented a finite element model to predict the elasto-plastic behavior of a straight wire under pure bending loads. In our previous work [13], a methodology was presented to determine Holloman's material constants for homogenized electrical wires.

A new analytical formulation is presented in this paper for large deflection elastic-plastic bending of electrical wires. The overall bending behavior of the electrical wire is modeled based on Euler-Bernoulli beam theory [14]. The friction between conductors is defined using Amontons-Coulomb friction laws. The kinematic state of the wire is determined by comparing stick and slip axial forces acting on each conductor. Plasticity is modeled by treating the conductors as laminated composite beams with each lamina having a different bending modulus. The change in helix angle is neglected since the conductors are enclosed in insulation, which limits twisting of the helix and separation of the conductors. The total bending moment of the wire is the sum of moments in the individual conductors and the insulation.

An effective bending stiffness versus curvature relation is derived by homogenizing the wire as a cylindrical beam. The effective bending stiffness can then be used in digital manufacturing applications. An algorithm for packing circles in a larger circle [15] is used to determine the conductor layout in the wire cross section, i.e., the radial and angular positions of the conductors in the cross section. This is required as most manufacturers of electrical wires (e.g., [16]) specify only the number of conductors in a wire, but the arrangement of conductors needs to be known to model the forces acting on individual conductors. The packing algorithm and the analytical model together form a tool to automate the process of determining the bending stiffness for a large number of electrical wires based on their geometric and material properties.

Friction coefficients and the radial force exerted by the insulation are considered to be model parameters. A cantilever bending test is designed to characterize the wires with force at the free end recorded as a function of tip displacement. The cantilever bending test is simulated using the homogenized bending stiffness computed by the analytical model in a large deflection bending formulation to output force at the free end as a function of tip displacement. The model parameters are selected to minimize the error between the model output and experimental data. A 3D finite element simulation of the cantilever bending test is also conducted using Abaqus FEA® finite element analysis soft-

ware. The laminated beam assumption is validated by comparing the analytical model output with the FE model output.

Section 2 presents a nonlinear optimization method to evaluate the cross section layout of conductors and the nomenclature used to designate the conductors. The analytical formulation to model the elastic-plastic bending of helically stranded electrical wires is presented in Section 3. The evaluation of a homogenized bending stiffness and a large deflection formulation to simulate the cantilever bending of wires are presented in Section 4. Section 5 describes the cantilever bending test setup for model calibration and validation. The model has been calibrated and validated for wires with various conductor diameters, insulation thicknesses, types of conductors, and wire lengths and the results are presented in Section 6.

2. Wire geometry

In a wire, the positions of the conductors in the cross section affect the bending stiffness of the wire. Hence, in order to automate the process of defining conductor layouts for a large number of wire types and sizes in digital manufacturing applications, an algorithm is written for packing smaller circles in a larger bounding circle. The smaller circles represent the conductors and the larger circle represents the inner surface of the insulation. Initial values for the center coordinates of each conductor are guessed using a random number generator. The conductor layout is estimated by minimizing the elastic energy of the system, defined as the sum of distances squared.

Assume N smaller circles with equal radii r are to be packed in a larger bounding circle of radius R. The minimum distance between an i^{th} circle with center $(x_i, y_i; i = 1, 2, 3, ..., N)$ and a j^{th} circle with center $(x_i, y_i; j = 1, 2, 3, ..., N)$ is given by

$$d_{ij} = \begin{cases} 2r - \sqrt{(x_i - x_j)^2 + (y_i - y_j)^2} & \text{if } \sqrt{(x_i - x_j)^2 + (y_i - y_j)^2} < 2r \\ 0 & \text{otherwise.} \end{cases}$$
(1)

The minimum distance between the i^{th} circle and the bounding circle with center at the origin (0, 0) is given by

$$d_{i0} = \begin{cases} r - R + \sqrt{x_i^2 + y_i^2} & \text{if } \sqrt{x_i^2 + y_i^2} + r > R \\ 0 & \text{otherwise.} \end{cases}$$
 (2)

Assuming a unit proportionality constant, the potential energy of the i^{th} body is given by

$$U_i = d_{i0}^2 + \sum_{j=1, j \neq i}^{N} d_{ij}^2, \tag{3}$$

and the total potential energy U of the system is given by

$$U = \sum_{i=1}^{N} U_i. \tag{4}$$

Conductor centerline coordinates are solved by multi-variable optimization of $U(x_1,y_1,x_2,y_2,\ldots,x_N,y_N)$ using the MATLAB® function *fminunc*. This function uses a quasi-Newton search method to find the function minimum; the search direction is determined by estimating the approximate Hessian matrix using the Broyden—Fletcher—Goldfarb—Shanno (BFGS) formula. Initial values of the center locations are randomly chosen such that conductor centers are within the insulation as shown in Fig. 2(a). The final conductor arrangement after packing is shown in Fig. 2(b). Comparisons between the estimated conductor arrangements and actual wire cross sections for 7-conductor and 19-conductor wires are shown in Fig. 3.

The wire conductors are sorted into groups based on the radial distances of the conductor centerlines to the wire centerline. Here, the number of groups equals the number of layers in the helix. For simplicity, a

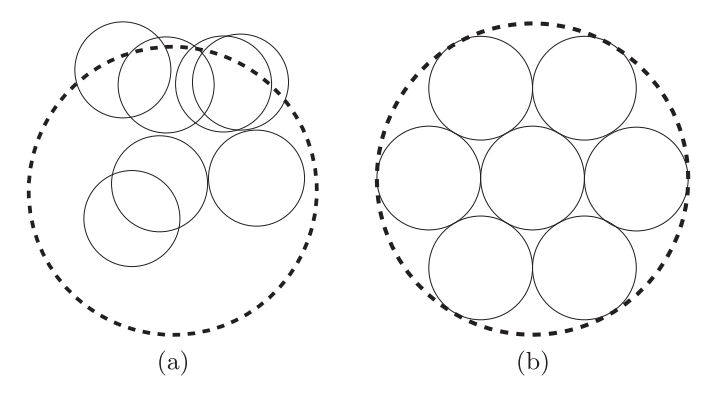


Fig. 2. (a) Initial guess for conductor configuration; (b) optimized conductor configuration obtained using a circle packing algorithm. The dashed circle represents the inner surface of the insulation and the solid circles represent the outlines of the individual conductors.

 p^{th} conductor in a q^{th} layer is identified as $(p,\,q)$. The values taken by $(p,\,q)$ are

$$(p,q) = \begin{pmatrix} 1,1 & 1,2 & \dots & 1,Q \\ 2,1 & 2,2 & \dots & \vdots \\ \vdots & \vdots & \ddots & \vdots \\ N_1,1 & \vdots & \ddots & \vdots \\ & & N_2,2 & \ddots & \vdots \\ & & & \ddots & \vdots \\ & & & & N_Q,Q \end{pmatrix},$$
 (5)

with the columns representing the helix layers and the rows representing the conductors in a layer. For example, the 7-conductor wire shown in Fig. 3(a) has one core and one layer with 6 conductors, so Q = 1 and $N_1 = 6$. Similarly, for the 19-conductor wire shown in Fig. 3(b), Q = 2, $N_1 = 6$, and $N_2 = 12$. In Fig. 3(b) there is a slight mismatch between the calculated and actual positions of the conductors in the second layer. Hence, we applied the analytical model to both the algorithm-generated and true configurations and found that the difference between the model outputs was not significant. For modeling, the wire layout is oriented by defining the neutral axis by a vector connecting the wire centerline and the centerline for a randomly chosen conductor in the first layer. For the wires tested in this work (lay angles < 15°), no distortion in the conductor cross sections was observed in either FEA or optical measurements. However, for wires with larger lay angles, it is understood that the lay angle can have an effect on the cross section shape of the conductors. To account for this change in cross section shape, the algorithm can be modified to pack ellipses within a circle [17]. The algorithm above is restricted to conductors with equal diameters, but can be readily modified to model wires having layers composed of conductors with different diameters [18].

In this work, we have modeled and tested two types of wires: wires with circular conductors and wires with compacted conductors. For circular conductors, the cross section layout is estimated using the algorithm as described above. For wires with compacted conductors, the

algorithm is effective for determining the number of conductors in each layer by assuming circles with equivalent cross sections. However, once the number of conductors in each layer is determined, the actual shapes of the conductors are modeled by defining polygons to fit that number of conductors in the layer while preserving conductor area.

3. Stick-slip model of the conductor

An electrical wire's conductive core is made of helically wound metal conductors. Due to its stranded nature, a wire in bending exhibits two kinematic states: stick state and slip state. Initially, the wire is in a stick state and bends as a single beam. With increasing curvature, the axial forces induced in the conductors due to bending exceed the frictional force and the conductors start to slip against adjacent surfaces, causing the wire to be in the slip state.

3.1. Stick state

Conductors in the stick state are modeled as Euler-Bernoulli beams and the axial strain in a conductor is the sum of responses from torsion, elongation, and bending of the wire. The axial strain in the $p^{\rm th}$ conductor in the $q^{\rm th}$ layer is given as

$$\epsilon_{p,q} = \kappa_w r_q \sin \theta_{p,q} \cos^2 \alpha_q + \epsilon_w \cos^2 \alpha_q + \tau_w r_q \sin \alpha_q \cos \alpha_q, \tag{6}$$

where κ_w, ϵ_w , and τ_w respectively denote curvature, elongation, and twist in a wire, r_q is the distance from the wire center to the $q^{\rm th}$ layer, $\theta_{p,q}$ is the angular position of the conductor from the x-axis, and α_q is the lay angle of the $q^{\rm th}$ layer. Multiplying (6) with conductor axial rigidity (EA)s gives the axial force as

$$T_{p,q} = (EA)_s \left(\kappa_w r_q \sin \theta_{p,q} \cos^2 \alpha_q + \epsilon_w \cos^2 \alpha_q + \tau_w r_q \sin \alpha_q \cos \alpha_q \right). \tag{7}$$

The wires are assumed to be under pure bending. Hence, the wire elongation and twist are neglected and the conductor axial force $T_{p,q}$ in (7) is directly proportional to r_q , the radial distance of the conductor centerline from the wire centerline. Therefore, slip begins in the conductors farthest from the neutral plane and progresses towards the center.

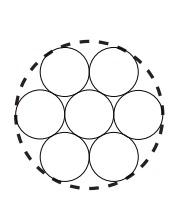
3.2. Slip state

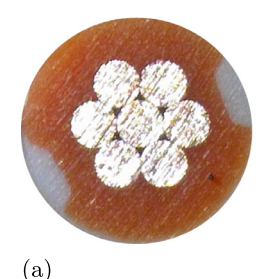
In the slip state, the Amontons-Coulomb friction model is used to define the contact forces between conductors and between the conductors and the insulation. Helically wound wires have a small tangential gap between conductors in the same layer [9] due to imperfections from manufacturing or the loading process. Hence, only the contact forces between conductors of adjacent layers are modeled and contact forces between conductors in the same helix layer are neglected. A differential conductor element in the $q^{\rm th}$ layer is selected and is shown in Fig. 4. The static equilibrium equation is given by

$$dF_{p,q} - g_{p,q} - h_{p,q} = 0, (8)$$

$$dF_{p,q} - \mu_q H_{p,q} - \mu_{q-1} G_{p,q} = 0, (9)$$

where μ_q and $H_{p,q}$ are the friction coefficient and the normal force, respectively, between layer q and layer q+1. Similarly, μ_{q-1} and $G_{p,q}$ are





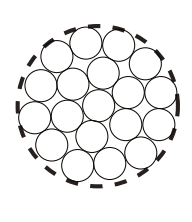




Fig. 3. Estimated and actual cross sections of a typical (a) 7-conductor wire and (b) 19-conductor wire.

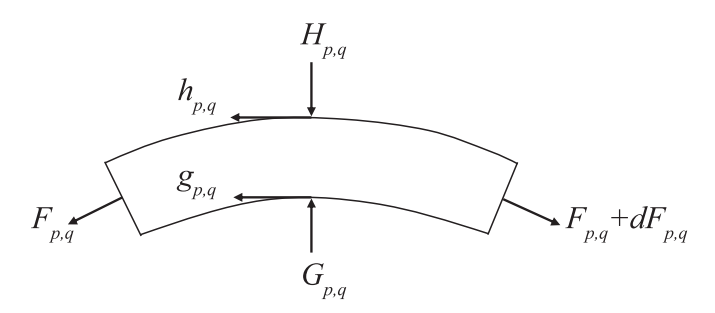


Fig. 4. Static force diagram for a differential element of the $p^{\rm th}$ conductor in the $q^{\rm th}$ layer subjected to an axial force $F_{p,q}$, normal forces $H_{p,q}$ and $G_{p,q}$ from adjacent layers, friction forces $h_{p,q}$ and $g_{p,q}$ resulting from relative sliding of adjacent layers, and the resulting increment in axial force dF.

the friction coefficient and the normal force, respectively, between layer q-1 and layer q.

The radial force exerted by the insulation F_{rad} is constant throughout the wire cross section. To satisfy equilibrium between layers, the force exerted by layer q on layer q-1 is given by

$$H_{p,q-1} = G_{p,q} \frac{N_q}{N_{q-1}}. \tag{10} \label{eq:10}$$

Substituting (10) in (9) and satisfying static equilibrium, the normal forces exerted on the q^{th} layer by the surrounding layers are given by

$$H_{p,q} = \sum_{k=q+1}^{Q} \left(F_{p,k} \sin \alpha_k \frac{N_k}{N_q} \right) + F_{rad} \frac{N_Q}{N_q}, \tag{11}$$

$$G_{p,q} = H_{p,q} + F_{p,q} \sin \alpha_q. \tag{12}$$

Substituting (11) and (12) in (9) we have the differential increment in axial force $dF_{p,q}$ as

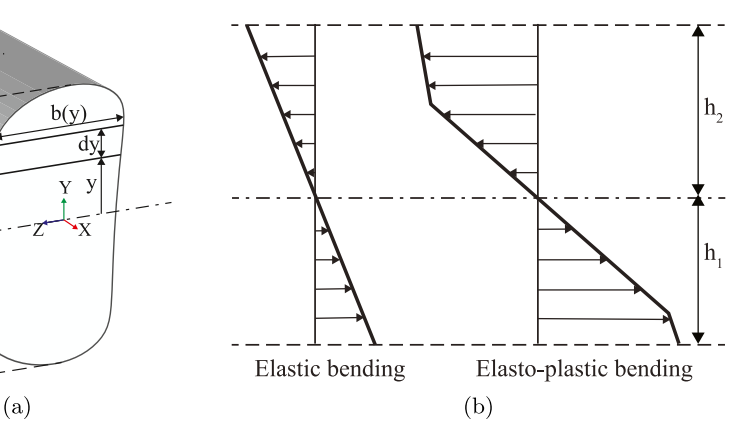
$$dF_{p,q} = \left(\mu_q + \mu_{q-1}\right) \left(\sum_{k=q+1}^{Q} F_{p,k} \sin \alpha_k \frac{N_k}{N_q} + F_{rad} \frac{N_Q}{N_q}\right) d\theta$$
$$+ \mu_{q-1} F_{p,q} \sin \alpha_q d\theta. \tag{13}$$

Solving (13) with initial condition $F_{p,q}(0)$, the frictional force $F_{p,q}$ in the p^{th} conductor in the q^{th} layer is given by

$$\begin{split} F_{p,q} &= \exp\left(\mu_{q-1} \sin \alpha_{q} \theta_{p,q}\right) \left(F_{p,q}(0) + \frac{\mu_{q} + \mu_{q-1}}{\mu_{q-1} \sin \alpha_{q}} B_{p,q}\right) \\ &- \frac{\mu_{q} + \mu_{q-1}}{\mu_{q-1} \sin \alpha_{q}} B_{p,q}, \end{split} \tag{14}$$

$$B_{p,q} = \sum_{k=q+1}^{Q} \left(F_{p,k} \sin \alpha_k \frac{N_k}{N_q} \right) + F_{rad} \frac{N_Q}{N_q}. \tag{15} \label{eq:Bpq}$$

h



In the solution procedure, for each increment in curvature κ , $T_{p,q}$ and $F_{p,q}$ are compared to determine if the conductor is in the stick or slip state and the minimum of $(T_{p,q},F_{p,q})$ is taken as the conductor axial force. Mathematically, the axial force is represented as

$$F_{p,q} = \begin{cases} T_{p,q} & \text{if } T_{p,q} < F_{p,q} \text{ (stick state)} \\ F_{p,q} & \text{otherwise (slip state).} \end{cases}$$
 (16)

3.3. Bending moment

The total bending moment induced in an electrical wire is the sum of moments in the conductors, moments in the insulation, and the moments induced by the conductors' axial forces. At a curvature κ , the total bending moment induced in a wire is given by

$$M = \sum_{q=1}^{Q} \sum_{p=1}^{N_q} EI_{p,q} \kappa + EI_{ins} \kappa + \sum_{q=1}^{Q} \sum_{p=1}^{N_q} F_{p,q} r_q \sin \theta_{p,q}.$$
 (17)

Here, $EI_{p,q}$ is the bending stiffness of the p^{th} strand in the q^{th} layer, EI_{ins} is the bending stiffness of the insulation, $F_{p,q}$ is the conductor axial force, and $r_q \sin \theta_{p,q}$ is the distance of the conductor center from the wire's neutral axis. In (17), $EI_{p,q}$ is given [10] by

$$EI_{p,q} = \frac{\cos(\alpha_q)}{2} EI_s \left(1 + \cos^2 \alpha_q + \frac{\sin \alpha_q}{1 + \nu_s} \right), \tag{18}$$

where EI_s is the bending stiffness of the conductor assumed as a straight cylindrical beam, and v_s is the Poisson's ratio of the conductor.

3.4. Effect of plasticity

During large deflection bending of a wire, the conductors undergo plastic deformation. The plastic zone begins when the maximum stress along the beam cross section exceeds the material's yield stress. The plastic zone spreads towards the neutral axis with increasing curvature. Fig. 5(b) shows the stress distribution in elastic and elasto-plastic regions.

A beam having only elastic stress distribution obeys Hooke's Law. However, in elasto-plastic stress distribution, the strain in the plastic region is not linearly related to the stress [19]. Therefore, the beam is assumed to have a laminated structure, with each lamina having different material properties. For a lamina with thickness dy, width b(y), and at a distance y from the neutral axis, the bending stiffness is given by

$$d(EI_s) = E(y)b(y)y^2dy, (19)$$

and integrating (19) across the beam cross section, the bending stiffness of the beam is given by

$$EI_s = \int_{-h_1}^{h_2} E(y)b(y)y^2 dy.$$
 (20)

Fig. 5. (a) Cross section of a generic beam showing a layer of differential thickness *dy*; (b) stress distribution across a beam cross section for elastic and elasto-plastic bending, showing stress reduction due to plasticity.

Here, the elastic modulus E(y) is the secant modulus calculated from the material stress-strain curve at a local strain $\epsilon_{xx} = y\kappa$. The conductors are typically made with ductile metals, hence the conductor is assumed to have the same stress-strain relationship in compression and in tension. For a cylindrical conductor with radius r, the bending stiffness given by (20) reduces to

$$EI_s = 2 \int_{-r}^{r} E(y) \left(\sqrt{r^2 - y^2} \right) y^2 dy,$$
 (21)

and discretizing the integral, we have

$$EI_s = 2\sum_{v=1}^{V} E_v \left(\sqrt{r^2 - y_v^2}\right) y_v^2 \Delta y.$$
 (22)

Here, V is the total number of laminae in the conductor cross section, E_{ν} is the elastic modulus of the ν^{th} layer, y_{ν} is the distance of the ν^{th} lamina from the neutral axis, and Δy is the lamina thickness ($\Delta y \ll R$). The bending stiffness given by (22) is for a straight cylindrical beam. Substituting (22) in (18) yields the bending stiffness of a helical beam. The total bending moment (17) is differentiated with respect to κ to give

$$EI_{w}(\kappa) = \sum_{q=1}^{Q} \sum_{p=1}^{N_{q}} EI_{p,q} + EI_{ins} + \sum_{q=1}^{Q} \sum_{p=1}^{N_{q}} \frac{dF_{p,q}r_{q}}{d\kappa}.$$
 (23)

At each value of curvature, the homogenized bending stiffness of the wire is evaluated using (23) and is recorded as a lookup table. The lookup table serves as a tool for use in digital manufacturing software to simulate wires as homogenized rods.

4. Large deflection formulation

In a wire subjected to small deflections, the curvature is $\kappa \approx \frac{d^2 y}{dx^2}$ and the bending moment is $M \approx E I_w \frac{d^2 y}{dx^2}$. For large deflections, elementary beam theory [20] gives the bending moment as

$$M = EI_w \kappa = EI_w \frac{\frac{d^2y}{dx^2}}{\left(1 + \left(\frac{dy}{dx}\right)^2\right)^{\frac{3}{2}}}.$$
 (24)

Here, EI_w is the homogenized bending stiffness of the wire. Expanding the denominator in (24) using binomial expansion and substituting M with P(l-x) we have

$$\frac{d^2y}{dx^2} = \frac{P(l-x)}{EI_w(\kappa)} \sum_{r=0}^{\infty} {1.5 \choose r} \left(\frac{dy}{dx}\right)^{2r},$$
(25)

where P is the point load applied at the free end of the cantilever, l is the projection of the cantilever beam on the x-axis, x is the distance from the free end as shown in Fig. 6, and $EI_w(\kappa)$ is a function of curvature κ

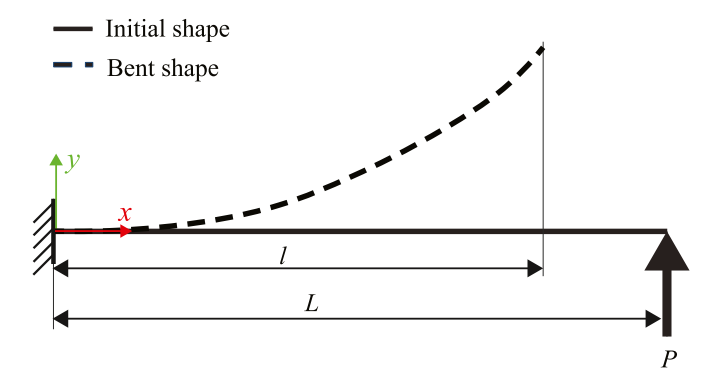


Fig. 6. Large deflection bending of a cantilever beam subjected to a point load at its free end, showing the beam length *L* and the projected length *l*.

as shown in (23). Solving the nonlinear differential Eq. (25) [21] using reversion [22], we derive the beam equation y(x) as

$$y(x) = \left(\frac{P}{2EI_w(\kappa)}\right) \left(-\frac{x^3}{3} + lx^2\right) + \frac{1}{2} \left(\frac{P}{2EI_w(\kappa)}\right)^3$$

$$\times \left(-\frac{x^7}{7} + lx^6 - \frac{12}{5}l^2x^5 + 2l^3x^4\right) + \text{higher order terms.}$$
 (26)

In the simulation procedure, the force P is increased in steps and at each increment, the shape of the beam is evaluated using (26). The bending stiffness EI_w varies with curvature and is determined from a look-up table of EI_w versus κ . Curvature at the fixed end, where slip initiates, is used to determine EI_w and at each increment of P, the bending stiffness is assumed constant along the beam curved length l. The tip displacement y(l) is recorded as a function of the tip force P.

5. Experiments

The bending responses of wires were measured to calibrate and validate model parameters such as friction coefficients and radial force exerted by the insulation. Two types of wires are tested; type A wires have uncompressed conductors and type B wires have compressed conductors. Dimensions, sample lengths, and cross section schematics of the wires tested are tabulated in Table 1. The wire diameters and the conductor areas are provided in the wire manufacturer specification sheet. The helix angle is determined by stripping the wire insulation and using a microscope to optically measure the angle between the helix and the wire axis. Type B wires were tested in two sample lengths to validate the model for different sample lengths.

This section describes the experimental setup and the procedure to test the samples. An inverted cantilever bending setup is designed to test the samples as shown in Fig. 7. One end of the wire sample is clamped in a fixture creating the fixed boundary condition, and the adapter is mounted on a shaft connected to a stepper motor. The other end is connected to a load cell with an aramid strand. The stepper motor provides displacement to the fixed end of the cantilever beam and simultaneously the tension in the aramid strand is measured by the load cell.

Fig. 8 shows the initial and bent shapes of a wire sample. The sample is displaced by 50 mm at 1 mm $\rm s^{-1}$. The aramid strand length is 760 mm and the tension in the strand is measured with a Cooper 2 g load cell. A dSPACE 1103 control box is used to control the stepper motor and to record the load cell measurements. Additionally, the shape of the wire sample during bending and the tip displacement are measured with a motion capture system. This avoids error due to the possibility of missing stepper motor steps at low speeds. The data is sampled at 10 kHz.

Table 1
Wire diameter, conductor area, number of conductors, lay angles of the conductors, sample lengths, and conductor layouts of the five types of wires tested. Type A wires have cylindrical conductors and type B wires have compressed conductors.

Wire	d _w (mm)	$A_c(\text{mm}^2)$	N_s	$\alpha_q(^\circ)$	L (mm)	Cross section
A1	1.4	0.37	7	12	85	
A2	1.6	0.56	7	12	85	
112	1.0	0.50	,	12	03	
А3	1.8	0.86	19	12, -15	85	
B1	1.1	0.35	7	12	85, 100	
B2	1.25	0.49	7	12	85, 100	

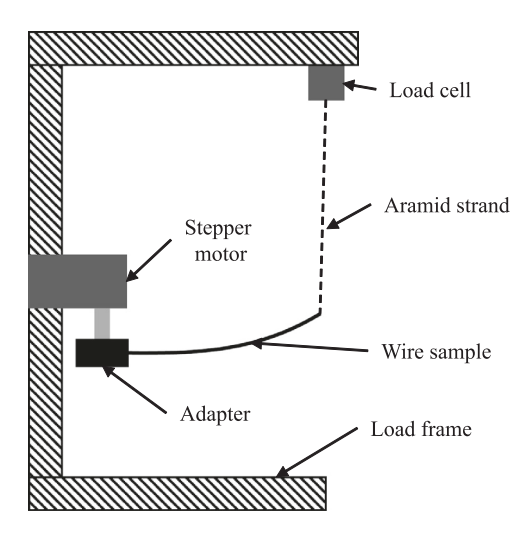


Fig. 7. Schematic representation of the experimental setup used for cantilever bend testing of electrical wires. The clamped end is displaced and the force at the free end is measured.

Three samples of each wire type and length are tested and the force versus tip displacement data for each test is recorded. For comparison with the analytical model, a 95% confidence interval is estimated based on the experimental data. The confidence limits at any displacement [23] δ for unknown population standard deviation are given by

$$F_{limits,\delta} = \overline{x}_{\delta} \pm t_{0.95,n} \frac{s}{\sqrt{n}},\tag{27}$$

where \overline{x}_{δ} is the mean force of all samples at displacement δ , n is the number of samples, $t_{0.95,n}$ is the t-statistic for n samples, and s is the standard deviation.

6. Results and discussion

The wires used in the analytical model development are made with copper conductors enclosed in PVC insulation. A stress-strain curve from Staller et al. [24] is used to model annealed copper and the elastic modulus of plasticized PVC is modeled as 1.225 GPa [25]. In the stick state, the wire has a constant bending stiffness since the conductors are in contact with each other and the wire bends as a single beam. In pure elastic bending, as the conductors start to slip against each other, the bending stiffness of the wire reduces towards a minimum value, at which point the friction between the conductors is negligible. However, in elasto-

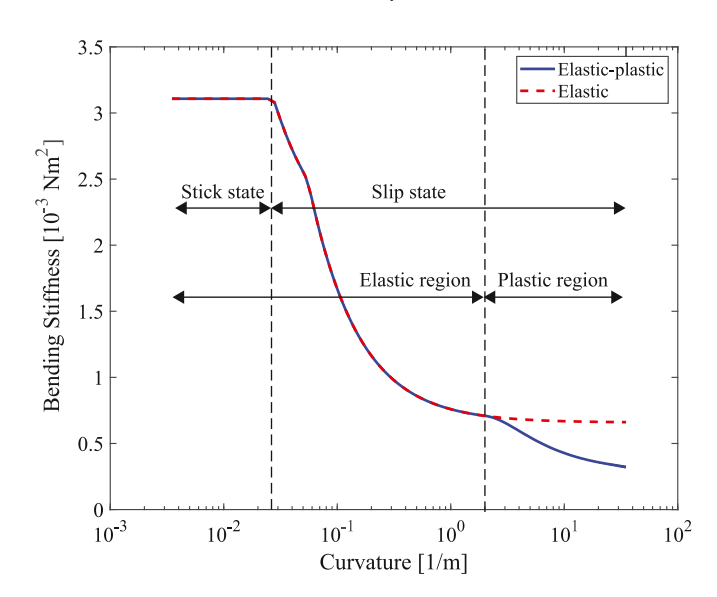


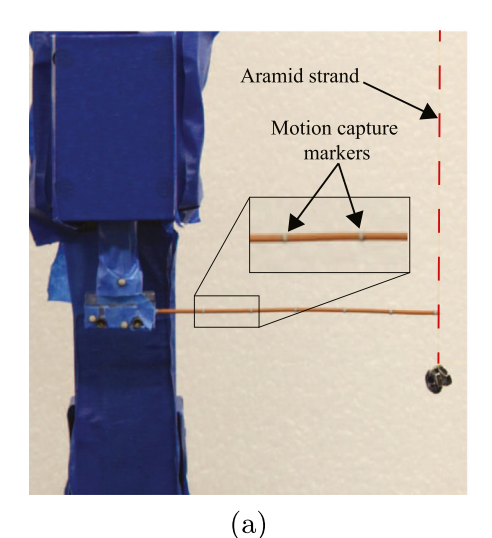
Fig. 9. Simulated bending stiffness versus curvature for wire A2 showing the two kinematic states for elastic and elasto-plastic models of wire bending.

plastic bending, the conductors start to undergo plastic deformation before attaining a fully slip state. The cantilever bend test presented in Section 5 is simulated based on the analytical model and the model parameters are calibrated by comparing the simulated force-displacement response with the test data.

The reduction in bending stiffness with increasing curvature for wire A2 is shown in Fig. 9. In the case of wire A2, the bending stiffness reduces by 77% from the stick to slip state and by another 55% from the slip state to the plastic region. The dashed line represents the variation in bending stiffness for a purely elastic model. The slip state represents the transition from partial to full slip. In the absence of plasticity, the bending stiffness reaches a constant value.

6.1. Model evaluation

The radial force exerted by the insulation F_{ins} , and the interlayer friction coefficients $(\mu_1, \mu_2, \dots, \mu_{N-1}, \mu_N)$ are identified as the model parameters. Because all the conductors are made with copper, interconductor friction coefficients are assumed to be equal, i.e. $\mu_1 = \mu_2 = \dots = \mu_{N-1} = \mu_s$, and the friction coefficient between the insulation and the outermost layer $(N^{\text{th}}$ layer) μ_N is designated as μ_p . The parameter values are evaluated by calibrating the model to minimize the error



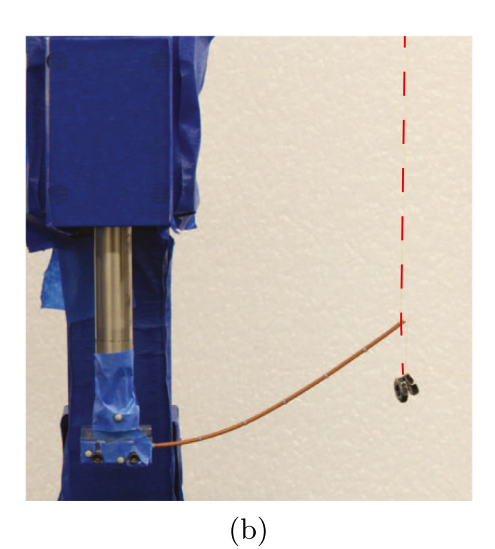


Fig. 8. (a) Initial and (b) final shapes of a wire sample during the cantilever bending test used for model development.

Table 2 Initial and optimized values of analytical model parameters: radial force exerted by the insulation (F_{rad}), inter-conductor friction coefficient (μ_s), and insulation-conductor friction coefficient (μ_p).

Parameter	F_{rad} (N)	μ_s	μ_p
Initial value	0.2	0.2	0.2
Optimized value	0.15	0.21	0.10

between the model output and the test data. For minimizing the error, an objective function is defined with μ_s , μ_p , and F_{rad} as the function variables and is given by

$$\epsilon = \sum_{i=1}^{n} \left[F_{m,i} \left(\mu_s, \mu_p, F_{rad} \right) - F_{e,i} \right]^2, \tag{28}$$

where ϵ is the error sum of squares (SSE), n is the total number of observations, $F_{e,i}$ is the force measured at displacement d_i , and $F_{m,i}$ is the force evaluated by the model at displacement d_i . Multivariable unconstrained optimization of the objective function using MATLAB® function fminunc solves for $(\mu_s, \ \mu_p, F_{rad})$ such that the objective function ϵ attains a minimum. Table 2 summarizes the initial and optimized values of the three model parameters. Data from testing wire A2 is used for model calibration and the data from testing other wires is used for model validation.

The measured and the simulated forces are normalized against the maximum overall recorded force and plotted versus tip displacement, as shown in Fig. 10(a). The wire shape is compared at six discrete tip displacement intervals and the measured and the simulated wire shapes are shown in Fig. 10(b). For each displacement interval, dots represent the motion capture markers on the experimental sample, the dashed line represents a polynomial fit of the markers, and the solid line represents the shape of the beam simulated by the analytical model. The difference in initial profiles between the measured sample shape and simulated beam shape is due to variability in preparing the wire sample. Fig. 10 shows that the model output agrees well with the experimental measurement.

The bending stiffnesses of wires A1, A2, and A3 are shown as a function of curvature in Fig. 11. As expected, the bending stiffness is highest for wire A3 which has the largest diameter. The stick-to-slip transition in wire A3 occurs over a higher range of curvature due to the larger number of conductors.

Fig. 12 (a) and (b) show the measured force and the simulated force versus tip displacement for wires A1 and A3. Wire A1 and A2 samples are 85 mm long, and wire A3 samples are 120 mm long. Wire A3 samples are longer to reduce the maximum force measured, due to the load cell capacity limit. The maximum tip displacement is 50 mm for all of the wire types. Therefore, the force observed at 50 mm displacement for wire A3 is lower than that for wires A1 and A2.

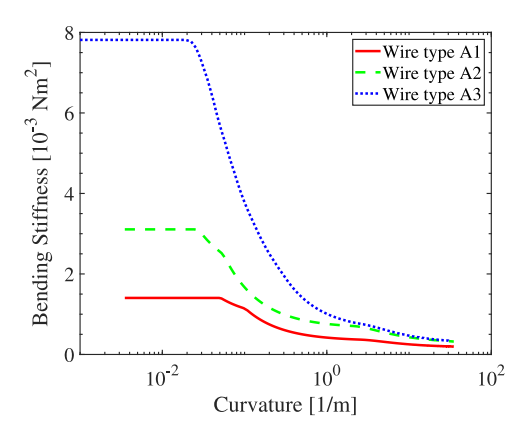


Fig. 11. Bending stiffness versus curvature for the three type A wires showing the difference in stick, slip, and plastic regions of the wires. Wire A3 has a more gradual transition from stick to slip state due to having two layers compared to a single layer for wires A1 and A2.

Table 3 Sum of squares errors (SSE) and root mean square errors (RMSE) for the analytical model relative to experimental measurements. All of the wire types have an error $\ll 1$, indicating that the analytical model provides a good fit.

SSE	RMSE
0.0056	0.0059
0.0012	0.0021
0.0005	0.0020
0.0033	0.0037
0.0127	0.0057
	0.0056 0.0012 0.0005 0.0033

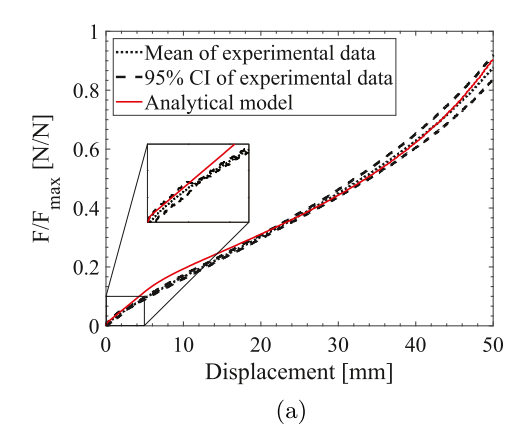
Wire type B samples were tested in two different lengths, 85 mm and 100 mm, to validate the independence of the analytical model on the sample length. Figs. 13 and 14 show the measured force and the simulated force as a function of tip displacement for wires B1 and B2, respectively.

Sum of squares errors (SSE) and root mean square errors (RMSE) are chosen as metrics to evaluate the model fit with respect to the experimental data. The SSE and RMSE values are calculated by

$$SSE = \sum_{i=1}^{n} (F_{model,i} - \bar{F}_{exp,i})^{2},$$
 (29)

$$RMSE = \sqrt{\frac{\sum_{i=1}^{n} \left(F_{model,i} - \bar{F}_{exp,i}\right)^{2}}{n}},$$
(30)

and are shown in Table 3.



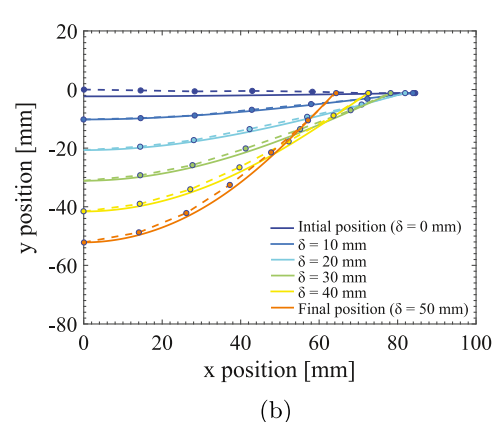


Fig. 10. (a) Measured and simulated force versus displacement curves for cantilever bending of wire A2 and (b) measured wire marker locations (dots), polynomial fits of marker locations (dashed lines), and the simulated wire shapes (solid lines) at various intervals of bending.

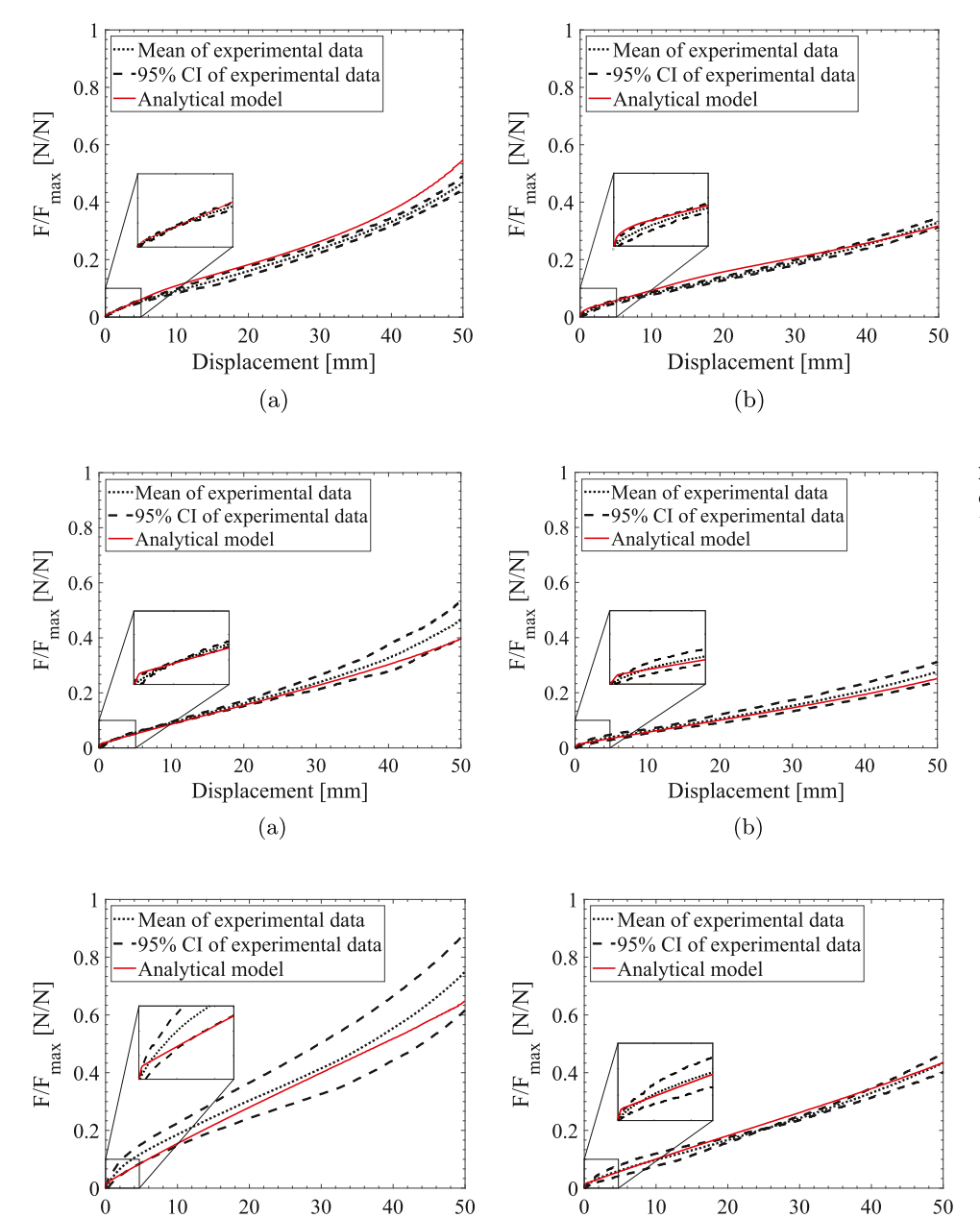


Fig. 12. Measured and simulated force versus displacement curves for (a) wire type A1 (sample length = 85 mm) and (b) wire type A3 (sample length = 120 mm).

Fig. 13. Measured and simulated force versus displacement curves for (a) 85 mm and (b) 100 mm long samples of wire type B1.

Fig. 14. Measured and simulated force versus displacement curves for (a) 85 mm and (b) 100 mm long samples of wire type B2.

For the evaluation of error metrics, the model output for each wire is compared against the experimental mean of the corresponding wire. Wire types A1, A2, A3, and B1 have SSE $\ll 1$ which shows that the model is a good fit. The analytical model output for wire type B2 is within the 95% confidence interval of the experimental data, but the SSE value is high because of a large variance in the test data.

Displacement [mm]

(a)

6.2. FEA of wire bending

Due to the high computational costs associated with performing high-fidelity simulations of stranded electrical wire bending, only wires A2 and B2 were chosen for the FEA study in Abaqus FEA®. The geometry, FE mesh, and deformed shapes of these wires are shown in Fig. 15. The conductors are discretized using 8-node hexahedral elements, where a custom Python script was developed for meshing compressed conductors in wire B2. The PVC insulation is meshed using 8-

node 3D continuum shell elements, which account for the insulation thickness the same way as 3D solid elements. The conductor cross section is discretized into 10 elements and the aspect ratio of each element is less than 3. An explicit integration scheme with a mass scaling factor of 20 is used to perform the simulation. Note that the mass scaling factor and the mesh size were chosen after a parametric study to ensure kinetic forces are insignificant, i.e., less than 5% of inertia forces at each time increment. In the cantilever bending simulation, one end of the wire is fixed by constraining all degrees of freedom, while the other end is vertically displaced. The friction coefficients, radial force exerted by the insulation, material properties, and geometrical properties are the same as those used with the analytical model.

Displacement [mm]

(b)

Fig. 16 shows the measured force, simulated force, and analytical model output force as a function of tip displacement for wires A2 and B2.

Mesh

50

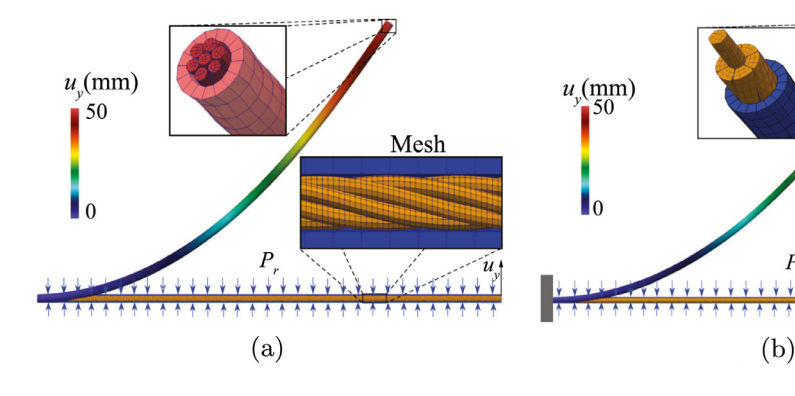


Fig. 15. FE models of wires (a) A2 and (b) B2, showing portions of the mesh and simulated bent shape of the wires.

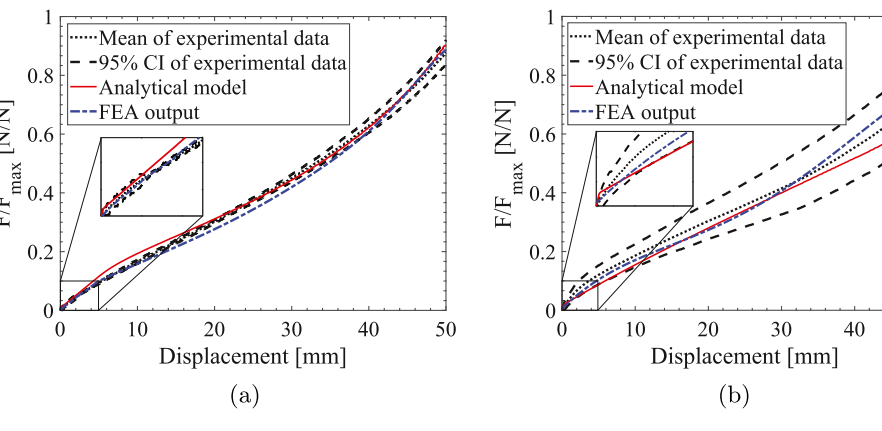


Fig. 16. Force versus displacement plots showing the experimental data, analytical model output, and FE model output for wire (a) A2 and (b) B2.

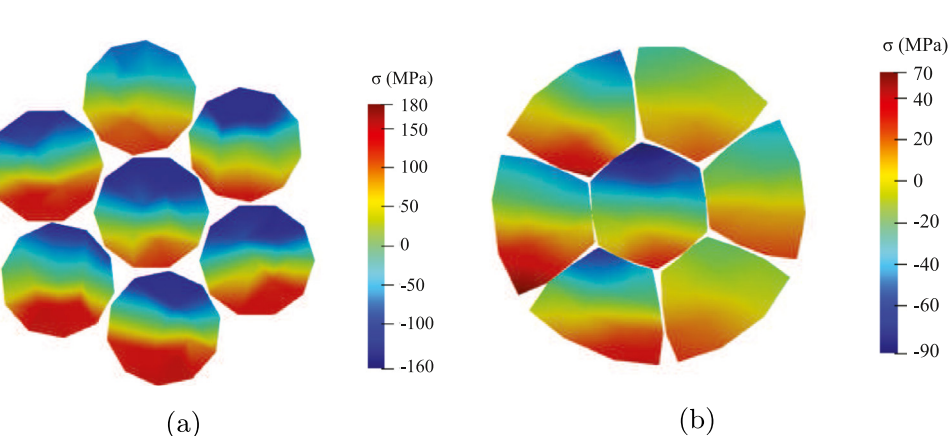


Fig. 17. Von Mises stress distribution at the fixed end for (a) wire type A2 and (b) wire type B2. The symmetric stress distribution in each wire supports the laminated stress distribution assumption presented in Section 3.4.

For wire A2, the RMS error between the FE model output and the experiments is 0.0031 for wire A2 and 0.0038 for wire B2. For the latter, there is a notable difference between the the force outputs of the FE model and the analytical model at higher deflections. This difference could be due to higher friction between conductors resulting from a larger contact area with the compressed wires, as well as the different cross section geometry of compressed conductors. In the analytical model, the compressed conductor cross sections are modeled as perfect polygons to simplify calculations, while the polygon edges are rounded in the FE model to improve the fidelity of simulations. However, outputs of both the analytical model and the FE model are still within the 95% confidence interval of the experimental data. The wavy nature of the FE model force output is caused by the mass scaling factor used to reduce the computational cost, as described by Taghipour et al. [13].

Fig. 17 shows that the stress profile in the conductors has a laminar form as proposed in Section 3.4. Stress profiles in wire A2 are fairly uniform for all the conductors. However, the stress profiles in wire B2 are biased about the horizontal plane of symmetry. It is conjectured that this bias is due to the polygonal shape of the conductor cross sections,

which interlock to resist twisting of the conductors, thus resulting in multiple sites of stress concentration.

Conclusion

A new analytical formulation is presented to characterize the large deflection elasto-plastic bending of electrical wires. The analytical model accounts for the helical structure of the conductors, friction between the conductors, the radial force exerted by the insulation on the conductors, and the plastic deformation of the conductors. The model parameters have been calibrated and validated against experiments such that the model output is within the 95% confidence interval of the test data. The analytical model output is also compared with 3D FE simulations for cantilever bending to further support the analytical model assumptions. The analytical model is successful in evaluating the bending stiffness of wires based on their geometrical and material properties. Hence, the analytical model can serve as a surrogate for experimental testing of electrical wires.

Future work will involve extending the analytical model to cable structures, where the wires are arranged in a bundle configuration.

Declaration of Competing Interest

None.

Acknowledgement

This work was funded by Honda R&D Americas, Inc. and also in part by an allocation of computing time from the Ohio Supercomputer Center (OSC). Partial support for SV was provided by the member organizations of the Smart Vehicle Concepts Center, a Phase III National Science Foundation Industry-University Cooperative Research Center (www.SmartVehicleCenter.org) operating under NSF Grant IIP 1738723.

References

- Derr J, Straub C, Ahmed S. Prediction of wiring harness reliability. SAE Trans 1987:218–26.
- [2] Pradhan A. Current trends in automotive wire harness design. In: Proceedings of the international conference on mechanical, production and automobile engineering (ICMPAE 2011), Pattaya, Thailand; 2011. p. 28–9.
- [3] Inoue T, Kawakita Y, Kawabe H, Kohtake Y, Furusyo M, Ohuchi K, et al. The development of a method to estimate the bending reliability of wiring harness. SAE Trans 2000;109(7):252–6.
- [4] Costello G. Analytical investigation of wire rope. Appl Mech Rev 1978:31(7):897–900.
- [5] Velinsky S. General nonlinear theory for complex wire rope. Int J Mech Sci 1985;27(7–8):497–507.
- [6] Lanteigne J. Theoretical estimation of the response of helically armored cables to tension, torsion, and bending. J Appl Mech 1985;52(2):423–32.

- [7] Papailiou K. On the bending stiffness of transmission line conductors. IEEE Trans Power Delivery 1997;12(4):1576–88.
- [8] Hong K, Kiureghian A, Sackman J. Bending behavior of helically wrapped cables. J Eng Mech 2005;131(5):500–11.
- [9] Inagaki K, Ekh J, Zahrai S. Mechanical analysis of second order helical structure in electrical cable. Int J Solids Struct 2007;44(5):1657–79.
- [10] Foti F, Martinelli L. Mechanical modeling of metallic strands subjected to tension, torsion and bending. Int J Solids Struct 2016;91:1–17.
- [11] Foti F, Martinelli L. An analytical approach to model the hysteretic bending behavior of spiral strands. Appl Math Modell 2016;40(13–14):6451–67.
- [12] Jiang W. A concise finite element model for pure bending analysis of simple wire strand. Int J Mech Sci 2012;54(1):69–73.
- [13] Taghipour E, Vemula S, Wang Z, Zhou Y, Qarib H, Gargesh K, et al. Characterization and computational modeling of electrical wires and wire bundles subject to bending loads. Int J Mech Sci 2018:140:211–27.
- [14] Labuschagne A, van Rensburg N, der Merwe AV. Comparison of linear beam theories. Math Comput Modell 2009;49(1–2):20–30.
- [15] Huang W, Xu R. Two personification strategies for solving circles packing problem. Sci China Ser E 1999;42(6):595–602.
- [16] Sumitomo Wiring Sytems Ltd. Wires and Cables for automobiles; 2016.
- [17] Kampas F, Pintér J, Castillo I. Optimal packing of general ellipses in a circle. In: Modeling and optimization: theory and applications. Springer; 2016. p. 23–37.
- [18] Wang H, Huang W, Zhang Q, Xu D. An improved algorithm for the packing of unequal circles within a larger containing circle. Eur J Oper Res 2002;141(2):440–53.
- [19] Štok B, Halilovič M. Analytical solutions in elasto-plastic bending of beams with rectangular cross section. Appl Math Modell 2009;33(3):1749–60.
- [20] Timoshenko S. History of strength of materials: with a brief account of the history of theory of elasticity and theory of structures. Courier Corporation; 1983.
- [21] Pipes L. The reversion method for solving nonlinear differential equations. J Appl Phys 1952;23(2):202-7.
- [22] Ang M, Wei W, Teck-Seng L. On the estimation of the large deflection of a cantilever beam. In: Proceedings of the IECON'93., International conference on industrial electronics, control, and instrumentation, 1993. IEEE; 1993. p. 1604–9.
- [23] Dean A, Voss D, Draguljić D. Design and analysis of experiments, vol. 1. 2nd ed. Springer; 2017.
- [24] Staller O, Mitterbauer C, Mayr K. Tensile strengths and Young's modulus of thin copper and copper-nickel (CuNi44) substrates. Cent Eur J Chem 2008;6(4):535–41.
- [25] Grossman R. Handbook of vinyl formulating. John Wiley & Sons; 2008.